Progress in Additive Manufacturing
https://doi.org/10.1007/s40964-026-01805-6

RESEARCH

Influence of strut tapering and joint-node height on mechanical response of BCC lattices

David Liović[1] · Emanuele Vaglio[2] · Federico Scalzo[2] · Marina Franulović[1] · Giovanni Totis[2] · Marco Sortino[2]

Received: 23 March 2026 / Accepted: 27 May 2026

Abstract

This study investigates the tensile response of body-centered cubic (BCC) lattice structures with tapered struts manufactured from Ti6Al4V powder using a laser-beam powder bed fusion (PBF-LB) process. It quantifies how the end diameter (d_{end}), mid-span diameter (d_{mid}), and joint-node height (h) affect Young's modulus (E), 0.2% proof stress ($R_{\mathrm{p0.2}}$), and ultimate tensile strength (R_{m}). Experimental tensile tests performed on lattice specimens were combined with simulations based on the finite element method (FEM). A parametric dataset was created using results from finite element simulations and used to develop response surface regression models. The elastic and early plastic responses estimated numerically showed high agreement with experimentally observed responses, whereas the post-peak regime exhibited larger discrepancies associated with progressive failure and fabrication-induced variability. Increases in d_{mid} and d_{end} led to higher E, $R_{\mathrm{p0.2}}$, and R_{m}, with the largest gains observed when both diameters increased simultaneously. This indicates a strong geometric interaction. Joint-node height showed a secondary and geometry-dependent influence. All developed regression models explained more than 99% of the variability in FEM-estimated E, $R_{\mathrm{p0.2}}$, and R_{m}, capturing nonlinear diameter effects and their interaction. When compared with experimentally determined E, $R_{\mathrm{p0.2}}$, and R_{m}, the models explained 85%, 90%, and 88% of the variability in experimentally determined mechanical properties, respectively. Overall, the proposed framework and the developed regression models may serve as useful tools for early-stage unit-cell geometry screening in lattice structures with tapered struts within the investigated design space, while broader experimental validation remains necessary.

Keywords BCC unit-cell · Tapered struts · Additive manufacturing · Lattice structures · Mechanical properties · Finite element method

✉ David Liović
david.liovic@uniri.hr

Emanuele Vaglio
emanuele.vaglio@uniud.it

Federico Scalzo
federico.scalzo@uniud.it

Marina Franulović
marina.franulovic@uniri.hr

Giovanni Totis
giovanni.totis@uniud.it

Marco Sortino
marco.sortino@uniud.it

[1] University of Rijeka, Faculty of Engineering, Vukovarska 58, 51000 Rijeka, Croatia

[2] Polytechnic Department of Engineering and Architecture, University of Udine, Via delle Scienze 206, 33100 Udine, Italy

1 Introduction

Recent advances in additive manufacturing (AM) have expanded the design space of lattice structures by enabling geometries that are difficult to produce using conventional subtractive machining. This has enabled the production of lattice structures with tailored mechanical responses, supporting their growing application in automotive, aerospace, and biomedical engineering [1–4]. When lattices are integrated into load-bearing components, their mechanical response must be thoroughly understood to ensure reliable performance under service loading.

Most studies conducted on lattice structures have focused on compressive loading [5], reflecting the importance of these structures in energy absorption and load-bearing applications [3, 6–9]. However, when lightweight structural design is required, evaluation of tensile performance

Published online: 15 July 2026

is equally important [5, 10, 11]. Moreover, lattice structures are widely used in biomedical implants as bone substitutes [12, 13]. As bone is subjected to a range of loading conditions, including compression, tension, bending, shear, torsion, and their combinations, tensile characterization is crucial for clinical assessment [11].

By comparison, investigation of tensile behavior has received far less attention [5, 10]. One reason for this lies in the practical difficulties related to tensile testing of lattice specimens [10]. In addition, many studies have focused on the elastic response of lattice structures [14, 15]. This gap is pronounced for tensile loading, where both manufacturing constraints and test configuration can influence mechanical response and observed failure mechanisms.

From a manufacturing standpoint, tensile test specimens are commonly fabricated in vertical or near-vertical orientations to reduce distortion caused by residual stresses during manufacturing and to avoid internal support structures [16]. However, this increases build height, which in turn raises production time and cost [17].

To address tensile testing challenges, recent efforts have been made to standardize lattice tensile test specimens [15, 18]. Gebre et al. [15] used the finite element method (FEM) to design optimal porosity gradients in the transition zone, whereas Jung et al. [18] optimized the transition region to reduce specimen height and mitigate high stress concentrations. In such settings, optimizations based on FEM can be computationally intensive and time-consuming. Therefore, there is growing interest in incorporating representative volume element (RVE) modeling approaches [19]. Although RVE modeling with homogenization is widely used to estimate the effective mechanical response of periodic lattice structures [20], such approaches without further extension are less suited to responses governed by localization and instability, including damage initiation, progressive failure, and geometry-dependent fracture [14, 21].

In tensile loading, failure in lattices with body-centered cubic (BCC) unit cells often initiates at nodal regions and propagates through a finite number of neighboring unit cells [22]. This makes boundary conditions, specimen size, and geometric asymmetry important factors that are not considered by classical periodic homogenization frameworks.

To reduce stress concentrations at those critical nodal regions, geometric modification strategies can be implemented, such as adding spheres [9], fillets which act as smooth transitions [23], and curved struts [1]. Another approach to influence mechanical response, reduce anisotropy, and influence stress concentration regions is strut tapering [24].

Although these strategies aim to reduce stress concentrations and improve load transfer, they achieve this in different ways. Fillets and spheres mainly act as nodal reinforcements. They modify the local geometry in regions where high stress concentrations are expected. On the other hand, curved and tapered struts modify the stiffness distribution along the strut and affect the balance between bending- and stretch-dominated deformation. In tapered struts, the end and mid-span diameters may therefore have different roles. The end diameter affects load transfer near the nodes, whereas the mid-span diameter affects strut compliance and bending stiffness. However, the combined influence of these tapering parameters under tensile loading remains insufficiently characterized.

A recent study investigated the full mechanical behavior of lattice structures in both compression and tension by combining experiments and numerical simulations [25]. However, the relationship between unit-cell strut tapering parameters and tensile mechanical properties was not the primary focus of that study. In particular, the combined influence of strut end diameter, mid-span diameter, and joint-node height on Young's modulus, 0.2% proof stress, and ultimate tensile strength has not been systematically quantified for tapered BCC lattices.

This work addresses the identified gap by characterizing the tensile response of PBF-LB Ti6Al4V BCC lattice structures with tapered struts and by systematically relating unit-cell geometry to mechanical properties through finite element simulations and regression modeling. The novelty of the study is threefold. First, it focuses on tensile loading, whereas most previous studies on lattice structures have emphasized compressive behavior. Second, it examines the combined effects of d_{mid}, d_{end}, and h, enabling a more complete assessment of how tapering and node positioning jointly influence stiffness and strength. Third, it develops response-surface design equations for E, $R_{\mathrm{p0.2}}$, and R_{m} from a FEM dataset supported by experiments, thereby providing surrogate models for rapid geometry screening within the investigated design space and potentially supporting early-stage engineering design.

2 Experimental procedures

This section outlines the specimen geometry, parameters of the PBF-LB manufacturing process, applied annealing heat treatment, dimensional characterization of actual strut diameters after manufacturing, and tensile testing procedures used in this study.

2.1 Specimen geometry

In this study, lattice specimens consisting of $\sim 4.6 \times 5 \times 5$ body-centered cubic (BCC) unit cells were investigated, as illustrated in Fig. 1. Each unit cell had fixed dimensions of

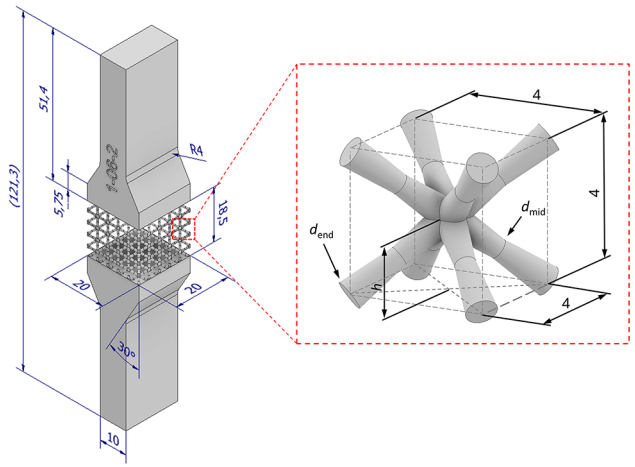

Fig. 1 3D model of the lattice specimen with BCC unit-cell configuration $d_{\mathrm{end}} = 1$ mm, $d_{\mathrm{mid}} = 0.6$ mm and $h = 2$ mm (1-06-2)

Table 1 BCC unit-cell configurations of manufactured lattice specimens

Specimen ID	d_{end}, mm	d_{mid}, mm	h, mm	No. of specimens
06-06-2	0.6	0.6	2	4
06-08-2	0.6	0.8	2	1
06-1-2	0.6	1	2	1
08-06-2	0.8	0.6	2	1
08-08-2	0.8	0.8	2	4
08-1-2	0.8	1	2	1
1-06-2	1	0.6	2	1
1-08-2	1	0.8	2	1
1-1-2	1	1	2	4
06-06-25	0.6	0.6	2.5	1
06-08-25	0.6	0.8	2.5	1
06-1-25	0.6	1	2.5	1
08-06-25	0.8	0.6	2.5	1
08-08-25	0.8	0.8	2.5	1
08-1-25	0.8	1	2.5	1
1-06-25	1	0.6	2.5	1
1-08-25	1	0.8	2.5	1
1-1-25	1	1	2.5	1
06-06-3	0.6	0.6	3	1
06-08-3	0.6	0.8	3	1
06-1-3	0.6	1	3	1
08-06-3	0.8	0.6	3	1
08-08-3	0.8	0.8	3	1
08-1-3	0.8	1	3	1
1-06-3	1	0.6	3	1
1-08-3	1	0.8	3	1
1-1-3	1	1	3	1

$4 \times 4 \times 4$ mm. As a result, the lattice section of the specimen exhibited an overall height of 18.5 mm, while the length and width were both equal to 20 mm. The selection of 4.6 unit cells in the loading direction enabled the placement of the extensometer within the solid region of the specimen and reduced the likelihood of failure at the interface between the solid part and the lattice structure. This configuration resulted in shortened struts within the boundary unit cells adjacent to the solid regions, thereby increasing their local stiffness and suppressing premature failure at the contact zones. Furthermore, a 5×5 arrangement of repeating unit cells in the transverse directions (width $\times$ length) was selected to reduce edge effects and therefore ensure a representative mechanical response.

The BCC unit-cell geometry is described using three parameters: strut end diameter (d_{end}), mid-span diameter (d_{mid}), and nodal joint height (h). In the experimental part, the nominal strut end (d_{end}) and mid-span (d_{mid}) diameters were varied between 0.6 and 1.0 mm. In the numerical part, the diameter range was extended to 1.2 mm to enlarge the parametric design space for regression modeling. In addition, the nodal joint height (h) was set to 2, 2.5, or 3 mm. Each unit-cell configuration is labeled using the following format: $d_{\mathrm{end}} - d_{\mathrm{mid}} - h$. This format is used throughout the study as the specimen identifier. An overview of all specimen identifiers and corresponding geometric parameters is provided in Table 1.

The selected tapering diameter range of 0.6−1.0 mm for additive manufacturing of lattice specimens was determined by both the limitation of the PBF-LB process and the geometric constraints of the BCC unit cell. Struts with diameters smaller than 0.6 mm are challenging to manufacture using the PBF-LB process, as they are more prone to defects due to their thin cross-section. This, in turn, reflects disproportionately on the mechanical response of the lattice. Such manufacturing defects limit the reliability and representativeness of the experimental measurements. Furthermore, the upper diameter limit for manufacturing was limited to 1.0 mm to mitigate excessive dross formation, particularly for configurations combining $d_{\mathrm{end}} = 0.6$ mm and $d_{\mathrm{mid}} = 1.0$ mm. Due to the inclined orientation of struts in BCC unit cells, larger tapering diameters favor the accumulation of dross. These regions typically have higher defect densities, surface irregularities, and increased roughness [26–28]. This, in turn, adversely influences the mechanical response and, consequently, the interpretation of the results. Furthermore, such surface textures make it difficult to accurately measure actual strut diameters. Note that for experimental validation, each geometric parameter was varied at three distinct levels (see Table 1), whereas in the numerical analysis, the design space was further extended to seven levels for the strut diameters, keeping three levels for joint-node height.

2.2 Specimen fabrication

A set of 36 lattice specimens incorporating various BCC unit-cell configurations was produced using the PBF-LB

Table 2 Bulk and contour parameters of the PBF-LB process used for specimen production

Region	P, W	v, mm/s	t, mm	h_D, mm	d, mm	E_L, J/mm
Bulk	225	1000	0.025	0.09	0.1	0.225
Contour	200	1750	0.025	–	0.07	0.114

Laser power (P), scanning speed (v), layer thickness (t), hatch distance (h_{D}), laser spot diameter (d), linear energy density (E_{L})

Fig. 2 Manufactured tensile test specimens featuring BCC unit cells integrated into a lattice

process. Fabrication was carried out on a Concept Laser M2 Cusing machine featuring a single-mode continuous-wave ytterbium-doped fiber laser with an emission wavelength of 1070 nm. Extra-low interstitial (ELI) Ti6Al4V Grade 23 powder served as the feedstock material. An island scanning strategy was employed during manufacturing, and the associated processing parameters are summarized in Table 2. Contouring was performed to improve the surface finishing. Representative images of the fabricated lattice specimens are presented in Fig. 2. The complete production of the specimen batch required 8 days and 11 h.

The annealing procedure was performed under an argon atmosphere to limit oxidation during heat treatment. The specimens were heated at a controlled rate of 3.5 °C/min until reaching 840 °C, where the temperature was held for 2 h. Subsequent slow cooling was performed within the closed furnace.

2.3 Dimensional accuracy after production

Typically, the PBF-LB process introduces a staircase effect on inclined surfaces. This results in strut diameters that deviate from their nominal CAD values and are generally larger than the CAD model specifies. To account for this, the finite element models of the fabricated lattice specimens were constructed by averaging the actual measurements of strut diameters rather than using the nominal diameters defined by the CAD model. Strut diameters were measured in two characteristic directions on the as-built strut cross-section. Due to the inclined orientation of the struts and the staircase effect inherent to the PBF-LB process, the manufactured cross-section deviated from the nominal circular CAD geometry. The quantities d_{minor} and d_{major} denote the smaller and larger measured diameters of the as-built strut cross-section, respectively. The effective diameter $d_{\mathrm{effective}}$ was calculated as the average of d_{minor} and d_{major} and was used as a simplified geometry correction in the corresponding FEM models. The corresponding measurements are summarized in Table 3. Strut diameters were measured twelve times prior to tensile testing using a digital caliper with a resolution of 0.01 mm, a repeatability of 0.01 mm, and a maximum measurement error of 0.02 mm. This approach provides a representative basis for comparing the mechanical response of the physical specimens and their simulated counterparts.

Table 3 Designed and actual strut diameters after PBF-LB

d_{designed}, mm	d_{minor}, mm	d_{major}, mm	$d_{\mathrm{effective}}$, mm
0.6	0.58 ± 0.02	0.98 ± 0.05	0.78 ± 0.21
0.8	0.78 ± 0.03	1.18 ± 0.04	0.98 ± 0.21
1	0.98 ± 0.02	1.41 ± 0.03	1.20 ± 0.22

Values are reported as mean ± standard deviation

In this study, repeated digital caliper measurements were considered sufficient. The objective was to obtain corrected diameter values for comparison with FEM counterparts, rather than a full local reconstruction of the manufactured geometry. However, this approximation does not include local irregularities, such as diameter variations along the strut length, ovality, surface roughness, adhered particles, and local defects introduced during PBF-LB. These features were therefore not modeled individually. Their influence is reflected only indirectly through the effective measured diameters.

It should be noted that this geometric correction was applied only for the purpose of comparison between actual specimens and their corresponding numerical counterparts. In contrast, all regression models were developed using solely data obtained from the numerical simulations performed on unit-cell configurations having strut diameters uniformly distributed at seven levels in the range between 0.6 mm and 1.2 mm, and three different node heights (2 mm, 2.5 mm, and 3 mm). The use of uniformly spaced diameter values promotes parameter identification in regression modeling, reduces potential estimation bias, and facilitates the detection of interaction effects. This, in turn, increases the reliability and robustness of the regression models developed.

2.4 Tensile testing

Improper specimen design or manufacturing-induced defects can lead to early failure at the solid-lattice interfaces due to stiffness discontinuities. One strategy to avoid this outcome is to gradually densify the lattice near these interfaces, thereby creating a smoother stiffness transition [27]. That approach requires attaching the extensometer directly to the lattice region. For the BCC lattice structures considered in this study, such attachment of the extensometer is challenging, as the only accessible locations are at the nodal regions. As the tensile load increases during the tensile test, these regions are subjected to both axial and rotational displacements. In combination with unavoidable geometric imperfections, this adversely influences strain measurements using a contact extensometer.

Therefore, the extensometer was attached to the solid region of the specimen. To make that possible, the lattice structures were designed to have approximately $4.6 \times 5 \times 5$ BCC unit-cells. This leads to slightly shorter struts at the solid–lattice interfaces, which in turn decrease stiffness jumps. This configuration promotes damage initiation within the lattice region, rather than at the solid-lattice interfaces, thereby ensuring reliable strain measurements.

Tensile testing was performed using a StepLAB electromechanical testing machine equipped with a 25 kN load cell. A crosshead speed was set to 0.01 mm/s. Strain measurements were obtained using an Epsilontech 3442-010 M-050 M-ST extensometer with a gauge length of 20 mm.

For specimens exceeding the 22 kN capacity of the StepLAB electromechanical testing machine, tensile tests were performed on a Galdabini Quasar 50 universal testing machine equipped with a 50 kN load cell and DANTEC digital image correlation (DIC) system. The same crosshead speed was used in this machine to ensure consistency. In addition to recording the stress–strain response, the DIC system was used to capture displacement fields in the solid regions of the lattice specimens, from which strain was subsequently calculated using data extracted with a virtual extensometer.

It should be noted that the experimental tests were primarily performed to provide comparative support for the numerical analysis across the investigated specimen configurations, rather than a statistically comprehensive validation with multiple repetitions for each configuration. Most configurations were tested using a single specimen, while repetitions were available only for a subset of configurations. In addition, a full mechanical response was not captured for specimen 1-1-3 due to limitations related to the tensile test machines used. Accordingly, the experimental results should be interpreted as limited verification, with the strongest support provided for trends in elastic and early plastic behavior.

3 Numerical analysis

Numerical simulations were performed using the Abaqus 2020 software package. The Abaqus/Explicit solver was selected to address the pronounced nonlinearities present in the analyzed lattice structures, including complex contact interactions, large local deformations, and progressive material damage. These features make the standard solver less robust, while the explicit formulation provides stable and reliable solutions for the conditions considered in this study. The finite element formulation and constitutive modeling approach described within this section are based on [29, 30].

3.1 Material modeling

The mechanical response of the lattice structures was simulated using an elastoplastic constitutive model with ductile damage implemented in Abaqus/Explicit. Plastic deformation was described using the von Mises yield criterion with isotropic hardening, while material degradation was introduced through a ductile damage formulation. This modeling approach was selected since the tensile response of the investigated lattices involves local yielding, damage initiation, and progressive loss of load-carrying capacity.

Damage initiation was defined using an equivalent plastic strain criterion. In this formulation, damage starts when the accumulated equivalent plastic strain reaches the critical value specified for damage initiation. After damage initiation, material degradation was described using a scalar damage variable D, which progressively reduces the effective stress according to:

$$\boldsymbol{\sigma} = (1 - D)\bar{\boldsymbol{\sigma}}, \tag{1}$$

where $\bar{\boldsymbol{\sigma}}$ denotes the effective undamaged stress tensor, while D is the scalar damage variable ranging from 0 for the undamaged state to 1 for complete material failure.

To reduce mesh dependence during damage evolution, a fracture-energy-based formulation was used. In this approach, the failure process is described through the energy dissipated during damage progression rather than only through the equivalent plastic strain at failure. The fracture energy G_{f} was calculated as:

$$G_{\mathrm{f}} = \frac{\sigma_{\mathrm{y0}} L(\bar{\varepsilon}_{\mathrm{f}}^{\mathrm{pl}} - \bar{\varepsilon}_{\mathrm{D}}^{\mathrm{pl}})}{2}, \tag{2}$$

where σ_{y0} is the yield stress at damage initiation, L is the characteristic element length, $\bar{\varepsilon}_{f}^{pl}$ is the equivalent plastic strain at failure, and $\bar{\varepsilon}_{D}^{pl}$ is the equivalent plastic strain at damage initiation. This formulation was used to provide a practical representation of stiffness degradation and failure initiation in the lattice struts while limiting mesh-dependent effects in the post-yield regime.

To fully characterize the elastoplastic response of the material and its damage evolution, the corresponding material parameters must be identified.

3.2 Material parameters

The mechanical properties used in the numerical modeling of the lattice structures were adopted from the study of Murchio et al. [31], who experimentally characterized 45∘-oriented struts with a nominal diameter of 0.6 mm using a DIC system. Based on these findings, the mechanical response of the lattice specimens was represented by a bilinear elastoplastic material model. The Young's modulus of the solid material was fixed at 80.3 GPa for all lattice configurations, corresponding to the properties reported for the 45∘ strut orientation [31]. A Poisson's ratio of 0.31 and a mass density of 4.432 g/cm^3 were adopted from [32, 33]. This strategy of keeping constant all mechanical properties for all specimen configurations was adopted to obtain a practical and simple modeling procedure across the design space, without performing additional recalibration steps for mechanical properties. The objective was therefore not to create calibrated material properties for each strut diameter, joint-node height, or local strut orientation, but to evaluate whether a single combination of mechanical properties can capture the main geometry-dependent trends across the investigated design space.

Following the conversion of the experimental results reported by Murchio et al. [31] to true stress–true strain form, the yield strength was determined to be 582.2 MPa, while the ultimate tensile strength reached 768.3 MPa at a plastic strain of 0.031 mm/mm. The fracture strain was assumed equal to this value, with stress triaxiality set to 0.33 and the strain rate fixed at zero. Damage evolution was governed by a fracture energy criterion that accounts for the characteristic element length. Accordingly, for an element size of 0.2 mm, the fracture energy G_f was computed using Eq. (2), resulting in a value of 0.36 N/mm.

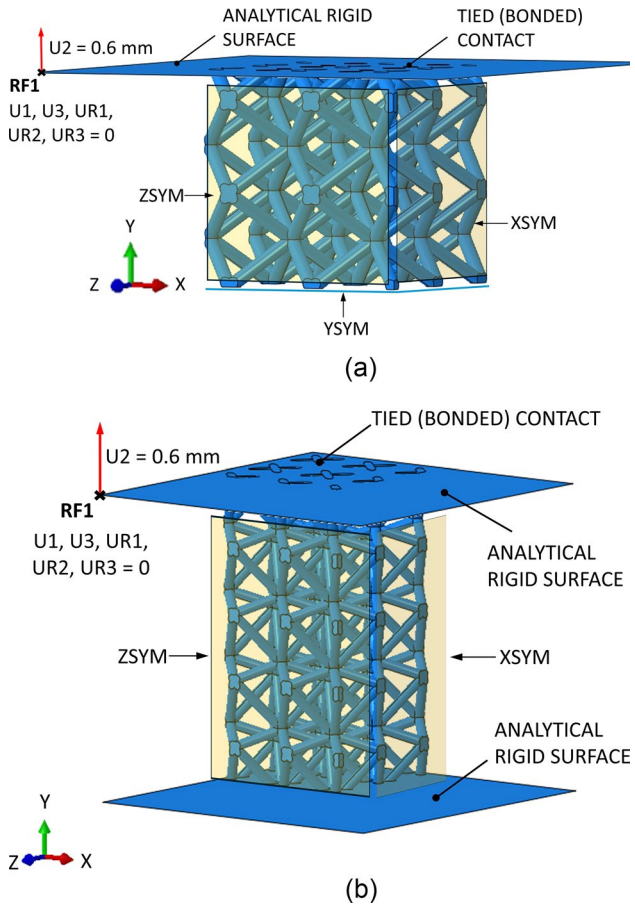

Fig. 3 Finite element representation of the lattice specimen, including the analytical rigid surface, reference point, applied boundary conditions, and constraints, for configurations with (**a**) symmetric, and **b** asymmetric BCC unit cells

3.3 Boundary conditions

The numerical model employed two distinct symmetry-based boundary-condition strategies, selected according to the geometric characteristics of the unit cells, as illustrated in Fig. 3. In the case of symmetric unit cells ($h = 2$ mm), symmetry constraints were enforced in the x-, y-, and z-directions (`XSYM`, `YSYM`, and `ZSYM`) as shown in Fig. 3a. This allowed the model domain to be reduced to one-eighth of the full specimen. For asymmetric unit cells (h = 2.5 or 3 mm), symmetry was imposed only along the x- and z-axes as can be seen in Fig. 3b. This resulted in a quarter-specimen representation.

The imposed displacement of the analytical rigid surface was set to 0.6 mm, while the remaining five degrees of freedom were fixed at a single reference point. To limit the introduction of inertial effects, the displacement was defined using a smooth step function. Computational efficiency was further improved by setting the total simulation duration to 1 s and applying a mass scaling factor of 1000. As a consequence, the numerical simulation time was reduced by approximately two orders of magnitude compared to the experimental tensile test, while the effective mass of the modeled specimen was proportionally increased.

A reference point associated with the analytical rigid surface was used to monitor the reaction force, displacement, and energy evolution throughout the simulation. Engineering stress and strain were subsequently determined during post-processing from the recorded reaction force and displacement data, using the nominal lattice cross-sectional area of 400 mm^2. A tied (bonded) contact interaction was defined to ensure full kinematic coupling between the lattice structure and the analytical rigid surface.

3.4 Mesh sensitivity analysis

A mesh convergence study was conducted to determine a suitable discretization of the unit cell using linear tetrahedral elements. Six mesh densities were evaluated using the 06-06-2 configuration, which represents the thinnest investigated lattice configuration and was therefore considered the most critical case with respect to mesh resolution and post-peak localization. Young's modulus, ultimate tensile strength, and the strain corresponding to a 30% post-peak stress drop were extracted from the numerical stress–strain curves, as illustrated in Fig. 4.

With increasing mesh refinement, Young's modulus and ultimate tensile strength reach stable values, while the strain corresponding to a 30% post-peak stress drop provides additional information on the stability of the early post-peak response. An optimal compromise between numerical accuracy and computational efficiency was obtained with approximately 6378 elements per unit cell, corresponding to an element size of 0.2 mm. This element size was therefore adopted for all subsequent simulations.

The suitability of symmetry boundary conditions for modeling lattice specimens under tensile loading was also examined. The use of symmetry allows a substantial reduction of the computational time, thereby decreasing the number of finite elements required and significantly reducing computational cost. The BCC unit cells with $h = 2$ mm investigated in this study have three orthogonal planes of symmetry, which enable the application

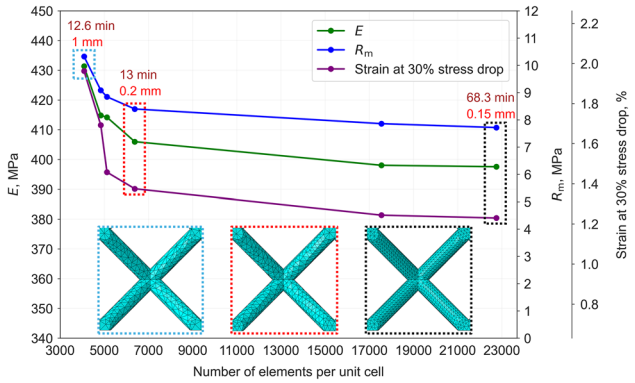

Fig. 4 Convergence of the estimated E, R_m, and the strain corresponding to a 30% post-peak stress drop as the mesh density per unit cell increases. Annotations in brown report the associated computation time, whereas annotations in red specify the element size used

of three-plane symmetry boundary conditions to lattice specimens composed of these cells. As a result, only one-eighth of the full specimen can be modeled, as illustrated in Fig. 5.

A comparison of the engineering stress–strain responses obtained with and without symmetry boundary conditions shows nearly identical behavior, with minor deviations observed only at higher stress–strain levels. These differences are attributed to the larger number of potential damage initiation sites present in the full-specimen model, which contains a greater number of unit cells and corresponding critical regions. Consequently, damage initiation and progression occur earlier in the model without symmetry, leading to premature failure. In contrast, the use of three-plane symmetry boundary conditions results in a slightly higher predicted ultimate tensile strength, with an increase of only 2.88% in R_m compared to the non-symmetric model.

The ratio of kinetic energy (E_{KE}) to internal energy (E_I) was monitored throughout each simulation, as time and mass scaling techniques were employed to reduce computational cost. As shown in Fig. 6a, the E_{KE} remained below 5% of the E_I for most of the loading history, indicating that inertial effects were negligible.

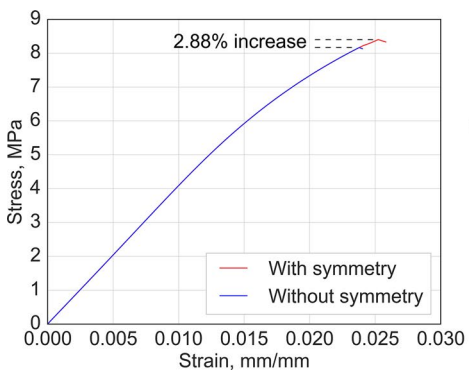

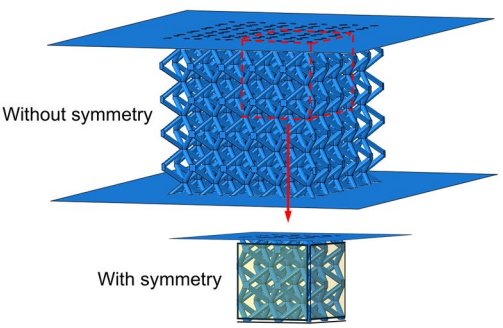

Fig. 5 Effect of symmetry boundary conditions on the engineering stress–strain response of the 06-06-2 lattice specimen

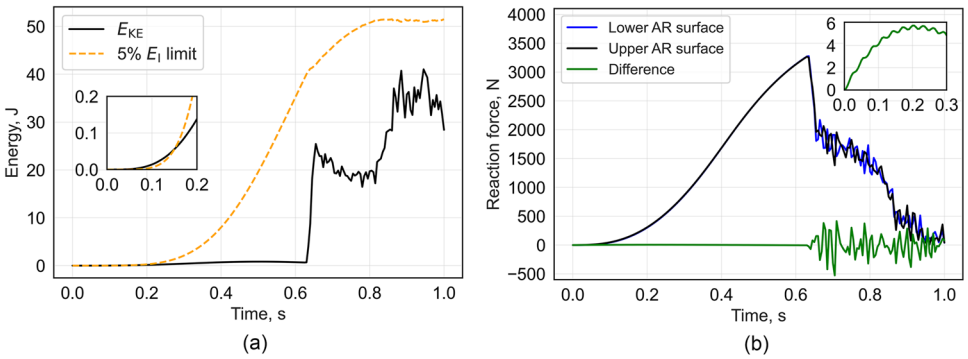

Fig. 6 **a** Time histories of internal and kinetic energy for the 06-06-2 lattice specimen under tensile loading, and **b** comparison of reaction forces at the upper and lower analytical rigid (AR) surfaces, including their difference

At the beginning of the simulation, for times up to 0.15 s, the kinetic energy E_{KE} slightly exceeds the commonly adopted threshold of 5–10% of the internal energy E_{I}. In this interval, however, E_{KE} remains below 0.1 J. Such low kinetic energy levels are achieved through the application of a smooth step displacement to the lattice specimen. Consequently, the contribution of inertial effects to mechanical response is minimal, as the associated inertial forces during the early loading stage are small, as illustrated in Fig. 6b

The influence of inertial forces caused by the use of time and mass scaling is demonstrated using the 06-06-2 lattice specimen without symmetry boundary conditions. This modeling setup allows the evaluation of reaction forces at both analytical rigid surfaces located at the upper and lower ends of the specimen. In the presence of elevated E_{KE}, pronounced inertial effects would manifest as a discrepancy between the reaction forces measured at these two surfaces. As shown in Figure 6b, the reaction force difference for the undamaged lattice reaches approximately 6 N at 0.2 s, which is 2% of the total reaction force at that given time. As time progresses, the reaction force difference decreases until damage initiation occurs at around 0.6 s, after which larger fluctuations and increased force differences are observed.

As damage propagates through multiple struts, fluctuations in E_{KE} become evident, reflecting a temporary rise in inertial forces. These effects do not affect the evaluated values of Young's modulus, 0.2% proof stress, or ultimate tensile strength, since these properties were determined from the initial linear portion of the stress–strain response, prior to the onset of damage.

4 Statistical analysis and modeling

Statistical analyses and response surface modeling were performed in R [34]. Three mechanical properties obtained from the FEM dataset were considered as response variables: Young's modulus (E), ultimate tensile strength (R_{m}), and 0.2% proof stress ($R_{\mathrm{p0.2}}$). All continuous geometric predictors were centered and scaled to the interval $[-1, 1]$.

A second-order response-surface regression framework was employed to model the dependence of the mechanical response on lattice geometry. The geometric parameters describing strut tapering (d_{mid} and d_{end}) were represented by a full quadratic polynomial, including linear, squared, and interaction terms. A full model was initially specified in which all quadratic response-surface terms were allowed to interact with the joint-node height h, thereby permitting both the magnitude and shape of the response surface to vary continuously with height. In compact form, the most general model can be written as:

$$\begin{aligned} Y = {} & \beta_0 + \beta_1 x_{\mathrm{mid}} + \beta_2 x_{\mathrm{end}} + \beta_{11} x_{\mathrm{mid}}^2 + \beta_{22} x_{\mathrm{end}}^2 + \beta_{12} x_{\mathrm{mid}} x_{\mathrm{end}} \\ & + \beta_3 x_h + \beta_{13} x_{\mathrm{mid}} x_h + \beta_{23} x_{\mathrm{end}} x_h \\ & + \beta_{113} x_{\mathrm{mid}}^2 x_h + \beta_{223} x_{\mathrm{end}}^2 x_h + \beta_{123} x_{\mathrm{mid}} x_{\mathrm{end}} x_h + \varepsilon. \end{aligned} \tag{3}$$

Here, Y denotes the mechanical response of interest, namely E, $R_{\mathrm{p0.2}}$, or R_{m}, while ε represents the random error term. The variables x_{mid}, x_{end}, and x_h denote the centered and scaled values of d_{mid}, d_{end}, and h, respectively. The initial model includes the full quadratic response surface in the two strut diameters, together with the additive linear effect of joint-node height and height-dependent interactions with the diameter-related terms. Models including a quadratic term in x_h were examined only as a sensitivity check and were not considered as candidate final models. Since h was investigated at only three levels, these data provide limited support for a robust interpretation of nonlinear height effects. Therefore, a linear term was used for h, and interactions with the diameter-related terms were included during model selection.

Several nested candidate models were compared during model selection. The additive height model included the full quadratic response surface in x_{mid} and x_{end}, with x_h included only as an additive linear term. The full interaction model allowed the diameter-related linear, quadratic,

and interaction terms to vary with x_h. Reduced interaction models were then obtained by removing non-significant height-dependent interaction terms from the full interaction model, while retaining the main effects and the full quadratic response surface in the two diameter-related predictors.

Nested analysis-of-variance (ANOVA) tests based on residual sum of squares were used to evaluate whether these reductions resulted in a significant loss of explanatory power relative to the full model. Model selection was further supported by the Akaike and Bayesian information criteria (AIC and BIC). Homoscedasticity was tested using the non-constant variance (NCV) test, and normality of studentized residuals was examined using the Shapiro–Wilk test. Robust standard errors (HC3) were used to test the model coefficients in the presence of possible heteroscedasticity, which may arise in response-surface models of mechanical data estimated using FEM.

Table 4 Experimentally determined mechanical properties of the lattice specimens

ID	E, MPa	$R_{p0.2}$, MPa	R_m, MPa
06-06-2	1048 ± 29	15.8 ± 0.4	18.0 ± 0.4
06-08-2	1741	20.4	23.8
06-1-2	2650	24.2	27.7
08-06-2	1657	19.6	23.3
08-08-2	2631 ± 87	33.3 ± 2.7	38.4 ± 1.5
08-1-2	3823	34.2	38.6
1-06-2	2562	31.4	33.2
1-08-2	4449	50.3	54.3
1-1-2	5336 ± 159	57.6	66.3
06-06-25	1016	13.6	16.7
06-08-25	1848	23.6	25.3
06-1-25	2280	26.5	29.1
08-06-25	1819	25.5	28.2
08-08-25	2447	31.4	35.3
08-1-25	4830	47.2	53.3
1-06-25	2607	32.8	38.3
1-08-25	3139	48.8	58.6
1-1-25	7303	69.1	71.9
06-06-3	1300	17	18.2
06-08-3	1542	18.8	20.7
06-1-3	2700	27.6	28.6
08-06-3	1879	25.1	26.1
08-08-3	3077	41	41
08-1-3	4693	47.3	50.1
1-06-3	2375	27.7	27.7
1-08-3	4663	58.7	59
1-1-3	7883	–	–

Values are reported as mean ± standard deviation when multiple specimens were tested. Single values correspond to configurations represented by one specimen. For configuration 1-1-3, the maximum load capacity of the testing setup was reached without failure. Therefore, only Young's modulus was determined. For configuration 1-1-2, Young's modulus was determined from three repetitions, whereas strength values were obtained from one specimen tested on the higher-capacity machine

5 Mechanical response: experimental versus numerical

The mechanical response varied widely across the investigated configurations. As summarized in Table 4, the investigated lattice configurations exhibited pronounced differences in mechanical response. An increase in the mid-span strut diameter d_{mid}, while maintaining a constant end diameter d_{end}, consistently leads to steeper stress–strain curves, reflecting higher values of Young's modulus, as summarized in Table 4. A similar trend is observed when increasing d_{end} at a fixed d_{mid}, confirming the positive influence of both tapering diameters on the elastic stiffness of the lattice structures.

The influence of the strut diameters on the strength-related properties is pronounced as well. Increasing either d_{mid} or d_{end} increases both $R_{p0.2}$ and R_m. This increase in load-bearing capacity is due to larger cross-sectional areas of the struts. The effect is even more pronounced when d_{mid} and d_{end} are increased simultaneously, resulting in the highest values of $R_{p0.2}$ and R_m.

The simultaneous increase in d_{mid} and d_{end} affects the tensile response in more than one way. At the same time, it increases the material volume and redistributes local stiffness within the unit cell. An increase in d_{mid} stiffens the strut along its length and reduces its bending compliance. On the other hand, an increase in d_{end} improves the load transfer near the nodal regions, where stress concentrations and damage initiation often occur. When both diameters are increased together, the unit cell becomes stiffer both along the strut body and at the nodal regions, which explains the pronounced synergistic increase in E, $R_{p0.2}$, and R_m. In mechanical terms, this combined effect shifts the response toward a more stretch- or axial-dominated regime, while simultaneously reducing the contribution of local bending and nodal compliance.

Although failure initiation was consistently observed near the nodal regions, the macroscopic stress required to reach this failure state is influenced by the stiffness of the entire strut, not only by the local node geometry. Increasing d_{mid} increases the axial and bending stiffness of the inclined struts, reduces their compliance, and limits local rotations at the nodes. Consequently, higher macroscopic stresses are required before critical plastic strain levels are reached near the nodal regions. Thus, $R_{p0.2}$ and R_m increase with d_{mid}, even though failure remains localized near the nodal regions.

In addition, h also influences E of the lattice structures. As reported in Table 4, an increase in h from 2 to 3 results in higher unit-cell stiffness, and consequently higher E for most configurations. It is worth noting that this effect is less pronounced for smaller d_{mid} and d_{end} values. This effect is

weaker than the effect associated with changes in the strut diameters on E.

Mechanically, this suggests that increasing h primarily modifies the position of the joint node and, consequently, the relative lengths of the connected struts rather than the load-bearing area of the struts along their full length. As h increases above the mid-height of the unit cell, the upper struts become shorter and the lower struts become longer, which increases the geometric asymmetry of the cell. This redistribution of strut lengths affects the local stiffness contributions of the inclined members and becomes more visible when d_{mid} and d_{end} are already relatively large, because the response is then governed less by strut bending and more by axial stretching of the unit-cell members.

For configurations with larger strut diameters, E increases with increasing joint height h, with the highest values observed at $h = 3$. This trend is related to stiffer nodal regions and reduced bending of the unit cells, which are asymmetric in that case. For smaller strut diameters, the effect of h on E is less pronounced, suggesting that the overall stiffness is less sensitive to unit-cell asymmetry.

Overall, an increase in h results in an increase in the lattice's E. However, this effect is secondary compared to the effect of strut diameters. The effect of joint height is more pronounced in the case of stiffer lattice configurations with larger strut cross-sections. In such configurations, the deformation mechanism is governed by axial loading rather than bending.

In this sense, the role of h differs from that of d_{mid} and d_{end}. While the tapering diameters directly increase the effective load-bearing cross-section and reduce compliance along the strut span, the joint-node height acts more indirectly by changing the node position, the symmetry of the unit cell, and the relative deformation contributions of the connected struts. This interpretation is also consistent with the broader rationale behind other geometric strategies reported in the literature, such as fillets, reinforced node transitions, and curved struts, which likewise aim to modify local compliance and stress transfer in critical nodal regions [1, 9, 23].

The FEM-estimated variations in E, $R_{\mathrm{p0.2}}$, and R_{m} across the parametric design space are summarized visually in the scatter plots shown in Fig. 7.

A comparison between 27 numerically estimated and experimentally observed stress–strain curves shown in Fig. 8 demonstrates a generally good agreement within the elastic and early plastic regimes across the investigated configurations. This agreement is most evident in the initial stiffness and in the relative ordering of the configurations with respect to $R_{\mathrm{p0.2}}$ and R_{m}. However, the level of experimental support is not uniform across the full design space, since most configurations were represented by a single tested specimen, and complete strength characterization was not available for configuration 1-1-3.

Deviations between experimental and numerical responses become more pronounced in the post-peak regime, where damage accumulation and progressive failure govern the mechanical behavior. In several configurations, the numerical model predicts a more abrupt post-peak degradation compared to the experimentally observed response, which typically exhibits a more gradual degradation. This behavior can be attributed to the inherent limitations of the modeling approach in representing distributed damage, local instability, and load redistribution effects arising from the complex lattice topology.

Additional sources of discrepancy may also arise from unavoidable manufacturing defects, dimensional inaccuracies, surface roughness, and material heterogeneity introduced during additive manufacturing. They may also arise from uncertainties in material parameter identification and from mesh sensitivity in the numerical simulations. In addition, the geometric correction used in the FEM models for each specimen was based on averaged effective diameters obtained by repeated caliper measurements, rather than on full-field geometric reconstruction. As a result, local shape deviations and surface features were not explicitly resolved, which may also contribute to part of the observed discrepancy between the experimental and numerical responses.

Nevertheless, the present results support the use of the numerical framework primarily for comparative evaluation of geometry effects and for estimation of the elastic and early plastic response within the investigated design space, rather than for full prediction of specimen-level failure behavior across all configurations.

A modest discrepancy in the elastic and early plastic response can be observed between the numerical predictions and the experimental results for configurations with larger strut diameters, such as 1-08-2, 08-1-25, 1-1-25, 1-08-3, and 1-1-3. The larger deviations observed for some configurations with $h = 3$ may also partly reflect the change in local strut orientations caused by the out-of-center node position. Since the numerical model used a single material parameter set based on 45°-oriented struts, orientation-dependent differences in strut-level mechanical properties were not explicitly represented. This behavior is expected as the material properties in the numerical model were set according to the data reported for struts with a nominal diameter of 0.6 mm [31]. Therefore, higher agreement between experimental and numerical results is obtained for diameters closer to 0.6 mm. This simplified approach, in which identical material properties were used for all configurations, was adopted to keep the modeling procedure simple and practical. Despite this assumption, the model captured dominant

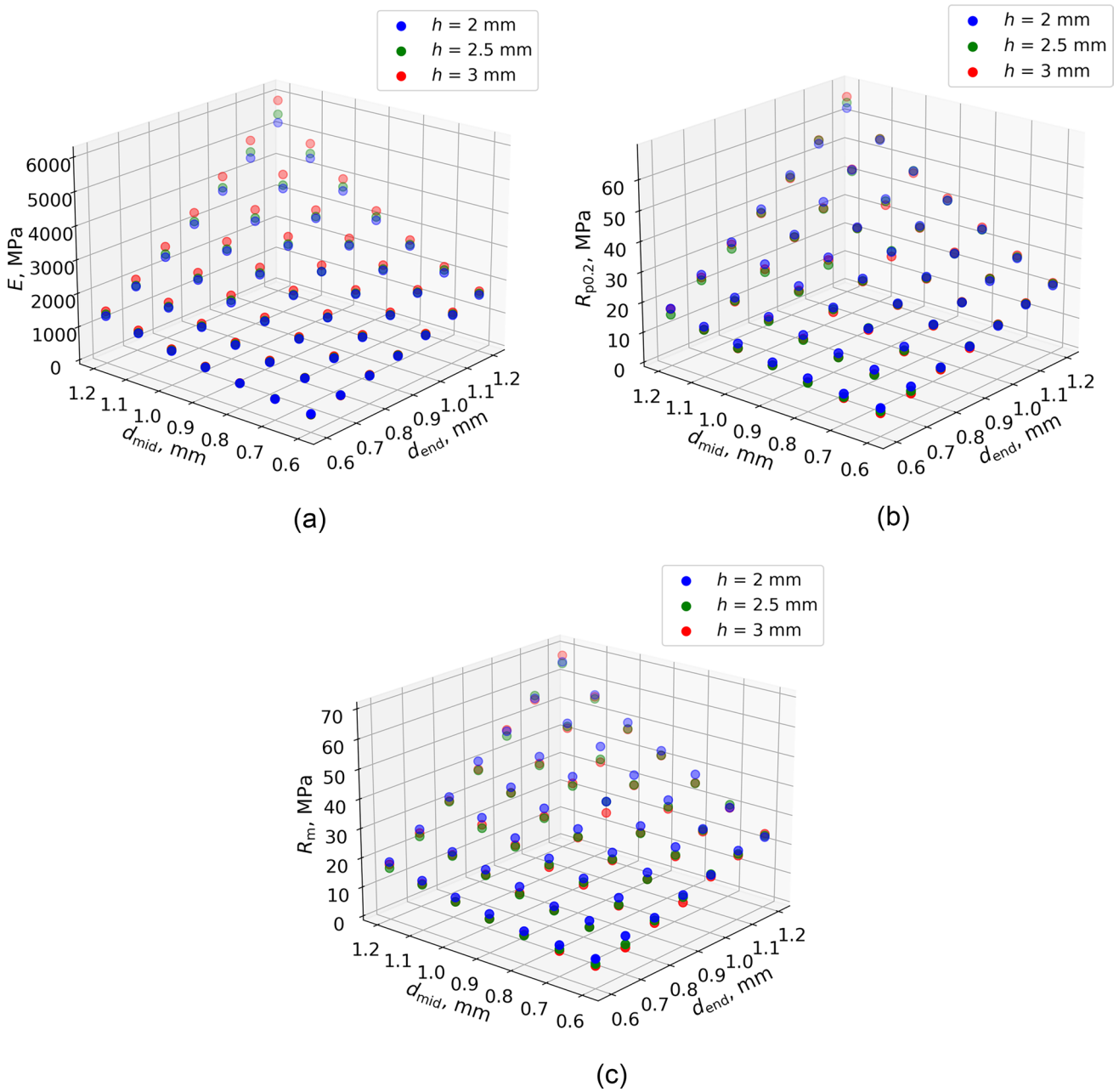

Fig. 7 Scatter plot showing FEM estimations of: **a** E, **b** $R_{\mathrm{p0.2}}$, and **c** R_{m}

trends with generally good agreement, particularly in the elastic and early plastic regimes. This indicates that the adopted mechanical properties provide a useful balance between simplicity and predictive capability.

Importantly, the ability of the numerical model to capture relative differences between configurations suggests that it can be effectively used for parametric optimization, even when absolute post-peak behavior is not fully reproduced.

In the numerical simulations, all lattice configurations exhibited failure at the nodal regions (Fig. 9), which is in agreement with the experimental observations. However, the numerical models consistently predicted planar failure. In contrast, the experimental specimens showed more complex fracture patterns. Specifically, several configurations exhibited a stepped fracture surface (e.g., 1-08-3, 1-08-2, and 1-1-25), whereas others failed along an inclined plane (e.g., 1-06-2).

The differences in lattice failure observed experimentally and numerically are attributed to differences between the two approaches. In particular, the FEM approach considers the lattice geometry using effective mean strut diameters. Furthermore, internal porosity,

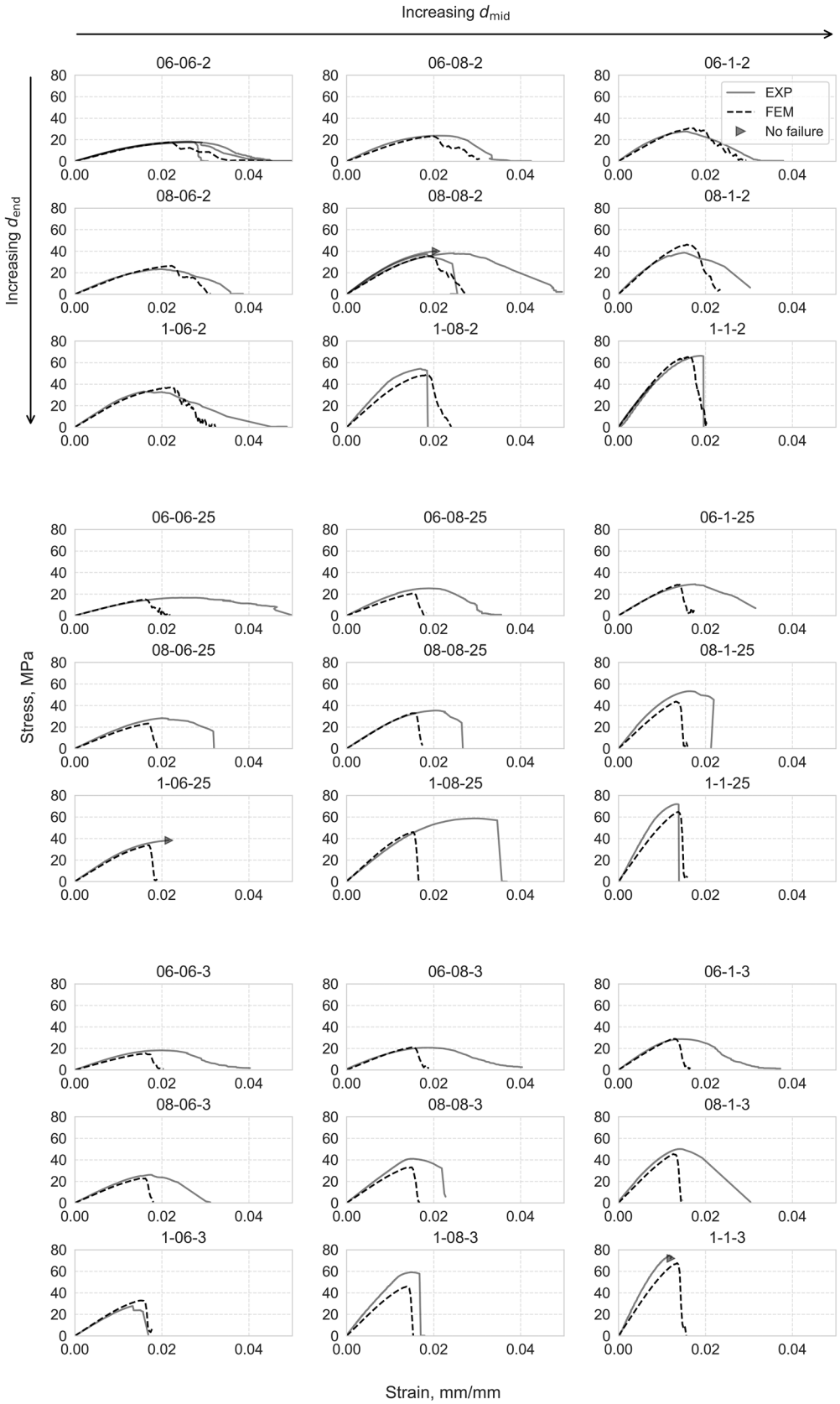

Fig. 8 Comparison between experimental and numerical stress–strain responses of lattice specimens with corrected strut diameters

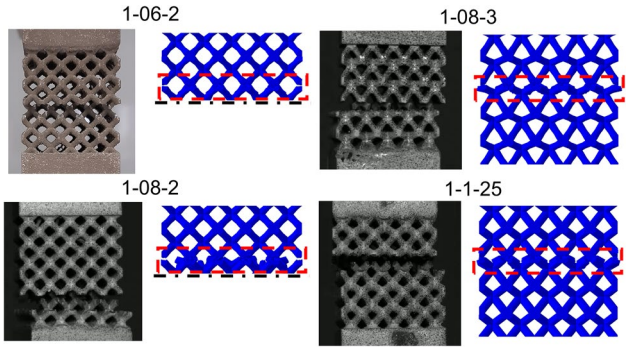

Fig. 9 Failure patterns of lattice configurations with corrected effective mean d_{end} and d_{mid} diameters using one-eighth (1-06-2 and 1-08-2) and one-quarter (1-08-3 and 1-1-25) symmetry

surface roughness, potential specimen distortion caused by residual stresses, and other defects caused by the PBF-LB process are completely neglected. In addition, minor specimen misalignment during tensile testing may introduce additional bending or torsion due to high clamping forces. This may further contribute to discrepancies between experimentally observed and numerically estimated mechanical responses.

Despite these differences in failure morphology, a good agreement is observed between numerically estimated and experimentally observed engineering stress–strain curves within the elastic and early plastic regime (see Fig. 8). The numerical approach, therefore, provides a useful basis for estimating relative differences in mechanical response among the investigated lattice configurations, particularly in the elastic and early plastic regimes. The proposed framework is therefore most suitable for estimating E, $R_{\mathrm{p0.2}}$, and R_{m}. A detailed reconstruction of mechanical response under damage remains outside its primary scope. On this basis, simplified regression models were developed as computationally efficient surrogate descriptions of the FEM response within the investigated design space.

In this respect, the present results are consistent with other geometry modification strategies reported in the literature, such as fillets, reinforced transitions, and curved struts [1, 9, 23]. Although these approaches differ geometrically from tapering, they all act by reducing local compliance and modifying stress transfer near critical nodal regions. The present results suggest that tapered strut design causes a related effect through the combined influence of span-wise stiffening by d_{mid} and strengthening in nodal proximity by d_{end}. At the same time, h further modulates the local constraint conditions in a secondary but mechanically meaningful way.

Table 5 Estimated coefficients of the response surface model for Young's modulus E

Term	Estimate	*SE* (HC3)	*t*	*p*
Intercept	1759.795	10.440	168.57	< 0.001
x_{mid}	1151.790	9.995	115.24	< 0.001
x_{end}	1256.709	10.225	122.91	< 0.001
x_{mid}^2	280.263	17.402	16.11	< 0.001
x_{end}^2	173.923	16.782	10.36	< 0.001
x_h	90.732	6.686	13.57	< 0.001
$x_{\mathrm{mid}} \times x_{\mathrm{end}}$	722.179	19.259	37.50	< 0.001
$x_{\mathrm{mid}} \times x_h$	84.034	12.831	6.55	< 0.001
$x_{\mathrm{end}} \times x_h$	67.266	13.055	5.15	< 0.001

6 Regression models

Within this section, developed regression models, their parameters, and statistical properties will be presented separately for E, $R_{\mathrm{p0.2}}$, and R_{m}.

The developed regression model for E captures 99.7% of the variability in the FEM-estimated response. Both tapering diameters show pronounced nonlinear behavior, with stiffness increasing more rapidly at larger diameter values. A pronounced positive interaction between x_{mid} and x_{end} indicates a strong synergistic effect, whereby simultaneous increases in both parameters lead to large stiffness gains. Joint-node height also affects stiffness, but its effect is geometry-dependent. In the selected model, x_h contributes through a linear term and through interactions with x_{mid} and x_{end}, indicating that the influence of joint-node height depends on the surrounding strut geometry rather than acting only as a uniform vertical shift of the response surface. Models including a quadratic term in joint-node height were examined as a sensitivity check, but this term was not retained because h was investigated at only three levels and was considered insufficiently robust for physical interpretation. The estimated model coefficients are reported in Table 5.

Model goodness-of-fit statistics and diagnostic test results are summarized in Table 6. Although formal tests indicate deviations from homoscedasticity and normality of the residuals, HC3 robust standard errors were used when assessing the estimated model coefficients.

Figure 10 shows the fitted response surface for E as a function of the centered and scaled predictors x_{mid} and x_{end}, displayed separately for each coded lattice height x_h. The contour lines and color gradients illustrate a smooth, monotonic increase in stiffness with increasing strut diameters, with a pronounced interaction between the two geometric parameters. Increasing x_h shifts the response surface upward and slightly modifies its slopes with respect to x_{mid} and x_{end}, reflecting the retained height-dependent

Table 6 Goodness-of-fit statistics and diagnostic tests for the response surface model of E

Metric	Value
Number of observations	147
Residual standard error (MPa)	62.48
R^2	0.9974
Adjusted R^2	0.9973
F-statistic	6682
F-test p-value	< 0.001
NCV test (χ^2, p)	37.24, $p < 0.001$
Shapiro–Wilk (W, p)	0.925, $p < 0.001$

Table 7 Estimated coefficients of the reduced response surface model for $R_{p0.2}$

Term	Estimate	SE (HC3)	t	p
Intercept	24.309	0.130	187.59	< 0.001
x_{mid}	12.541	0.103	121.27	< 0.001
x_{end}	15.351	0.101	151.33	< 0.001
x_{mid}^2	1.884	0.176	10.71	< 0.001
x_{end}^2	1.037	0.178	5.82	< 0.001
x_h	− 0.489	0.085	− 5.75	< 0.001
$x_{\mathrm{mid}} \times x_{\mathrm{end}}$	7.873	0.191	41.13	< 0.001
$x_{\mathrm{end}} \times x_h$	0.511	0.132	3.88	< 0.001
$x_{\mathrm{end}}^2 \times x_h$	0.443	0.219	2.03	0.045

interaction terms. This behavior is also clearly illustrated by the data shown in Fig. 7a.

The fitted response surface model for the $R_{p0.2}$ explains 99.8% of the variability in the FEM-estimated response. Both tapering diameters exhibit pronounced nonlinear effects, with $R_{p0.2}$ increasing at an accelerating rate toward larger strut diameters, as reflected by the positive quadratic terms. The coded end diameter (x_{end}) has a strong positive influence, as well as the mid-span diameter (x_{mid}), which contributes substantially through its linear term. A strong positive interaction between x_{mid} and x_{end} indicates a pronounced synergistic effect, whereby simultaneous increases in both parameters lead to substantially higher $R_{p0.2}$. The estimated coefficients (see Table 7) indicate that the influence of joint-node height on $R_{p0.2}$ was smaller than that of the two tapering diameters. In the selected model, x_h contributed through both an additive term and interactions with diameter-related terms, indicating that the effect of node position depends on the surrounding strut geometry rather than acting as an independent dominant factor.

Model selection for $R_{p0.2}$ was revised to avoid retaining height-dependent interaction terms that were not statistically informative. The full interaction model improved the fit relative to the additive height model, but several of its interaction terms showed high p-values and did not contribute meaningfully to the interpretation of the response surface. Therefore, a reduced interaction model was evaluated.

The selected reduced model retained the full quadratic response surface in x_{mid} and x_{end}, together with the additive effect of x_h, the interaction $x_{\mathrm{end}} \times x_h$, and the interaction $x_{\mathrm{end}}^2 \times x_h$. This reduced model provided the lowest information criteria among the compared alternatives (AIC = 324.5, BIC = 354.5), compared with the full interaction model (AIC = 326.4, BIC = 365.3), the additive height model (AIC = 348.4, BIC = 372.3), and the reduced model containing only $x_{\mathrm{end}} \times x_h$ (AIC = 328.6, BIC = 355.5). In addition, comparison with the full interaction model showed that removing the non-informative interaction terms did not result in a significant loss of fit $(F(3, 135) = 1.29, p = 0.282)$. The reduced model was therefore selected as the final model for $R_{p0.2}$. The estimated model coefficients are reported in Table 7.

Model goodness-of-fit statistics for the $R_{p0.2}$ model are summarized in Table 8. Although formal tests indicate deviations from homoscedasticity and normality of the residuals, HC3 robust standard errors were used when assessing the estimated model coefficients.

Figure 11 shows the fitted response surface for the $R_{p0.2}$ as a function of the centered and scaled mid-span and end diameters, displayed separately for each coded joint-node height. The contour plots reveal a strong nonlinear dependence of both tapering diameters, with a pronounced interaction effect leading to rapid increases in $R_{p0.2}$ when both diameters are large. Increasing *h* produces an overall downward shift of the response surface, while interactions with *h* allow modest changes in the magnitude of selected geometric effects across *h* levels. Overlaid FEM data points,

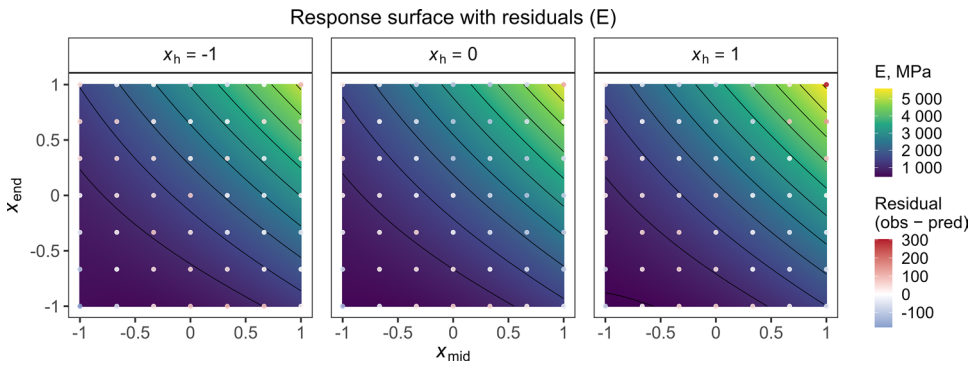

Fig. 10 Contour plot of the fitted response surface for E as a function of the centered and scaled geometric parameters. The overlaid points represent FEM simulation data, with point color indicating residuals between FEM-estimated values and response-surface predictions

Table 8 Goodness-of-fit statistics and diagnostic tests for the reduced response surface model of $R_{p0.2}$

Metric	Value
Number of observations	147
Residual standard error (MPa)	0.704
R^2	0.9975
Adjusted R^2	0.9974
F-statistic	6966
F-test p-value	< 0.001
NCV test (χ^2, p)	39.11, $p < 0.001$
Shapiro–Wilk (W, p)	0.912, $p < 0.001$

colored by residual magnitude, show no systematic spatial pattern, indicating that the response surface model adequately captures the dominant geometric trends across the investigated design space.

The regression model developed for the R_m captures 99.6% of the variability. Increases in tapering diameters have positive effects on R_m. In addition to pronounced linear effects, both diameters show significant quadratic terms, indicating a nonlinear strengthening trend toward larger strut diameters. A strong positive interaction between x_{mid} and x_{end} indicates a synergistic effect, whereby simultaneous increases in both parameters led to higher R_m.

Once the model selection procedure was completed, it was found that the inclusion of height-dependent interaction terms is justified. Relative to the additive height model, the reduced interaction model provided a significantly improved fit ($F(2, 138) = 9.03$, $p < 0.001$), whereas a further comparison indicated that the full interaction model did not improve fit relative to the reduced model ($F(3, 135) = 0.92$, $p = 0.433$). Information criteria supported the reduced interaction model: AIC favored the reduced interaction model (AIC = 402.8) over the full (AIC = 405.8) and additive models (AIC = 416.9), and BIC likewise favored the reduced interaction model (BIC = 432.7) over both the additive (BIC = 440.8) and full models (BIC = 444.7). Given the stronger complexity penalty of BIC and the goal of interpretable response surfaces, the reduced interaction model was selected as the final one. The estimated model coefficients are reported in Table 9.

Table 9 Estimated coefficients of the reduced response surface model for R_m (HC3 robust standard errors)

Term	Estimate	*SE* (HC3)	t	p
Intercept	25.235	0.163	154.42	< 0.001
x_{mid}	12.329	0.130	94.53	< 0.001
x_{end}	16.030	0.126	127.22	< 0.001
x_{mid}^2	1.926	0.226	8.50	< 0.001
x_{end}^2	1.013	0.216	4.69	< 0.001
x_h	− 1.596	0.186	− 8.59	< 0.001
$x_{mid}x_{end}$	7.568	0.229	33.11	< 0.001
$x_{mid}^2 x_h$	0.763	0.277	2.76	0.0066
$x_{end}^2 x_h$	0.683	0.264	2.59	0.0108

Table 10 Goodness-of-fit statistics and diagnostic tests for the reduced response surface model of R_m

Metric	Value
Number of observations	147
Residual standard error	0.918
R^2	0.9959
Adjusted R^2	0.9957
F-statistic	4239
F-test p-value	$p < 0.001$
NCV test (χ^2, p)	20.03, $p < 0.001$
Shapiro–Wilk (W, p)	0.969, $p = 0.002$

Model goodness-of-fit statistics for the R_m model is summarized in Table 10. Although formal tests indicate deviations from homoscedasticity and normality of the residuals, HC3 robust standard errors were used when evaluating the estimated model coefficients.

Figure 12 shows the fitted response surface for the R_m as a function of the centered and scaled mid-span and end diameters, displayed separately for each x_h. The contour plots reveal a dominant influence of tapering diameters on R_m, with consistently higher R_m values observed at larger diameters. Increasing x_h results in a downward shift of the response surface, with largely preserved interaction structure and only minor height-dependent curvature effects. The absence of systematic spatial patterns in the overlaid FEM data indicates that the model adequately captures the dominant geometric trends.

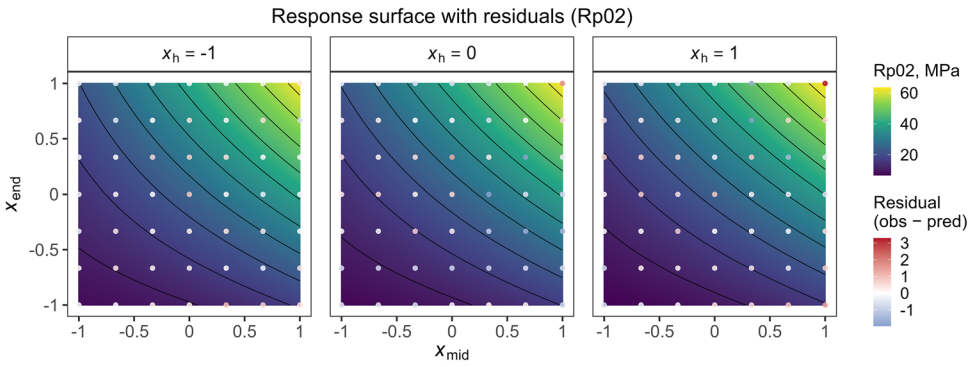

Fig. 11 Contour plot of the fitted response surface for $R_{p0.2}$ as a function of the centered and scaled geometric parameters. The overlaid points represent FEM simulation data, with point color indicating residuals between FEM-estimated values and response-surface predictions

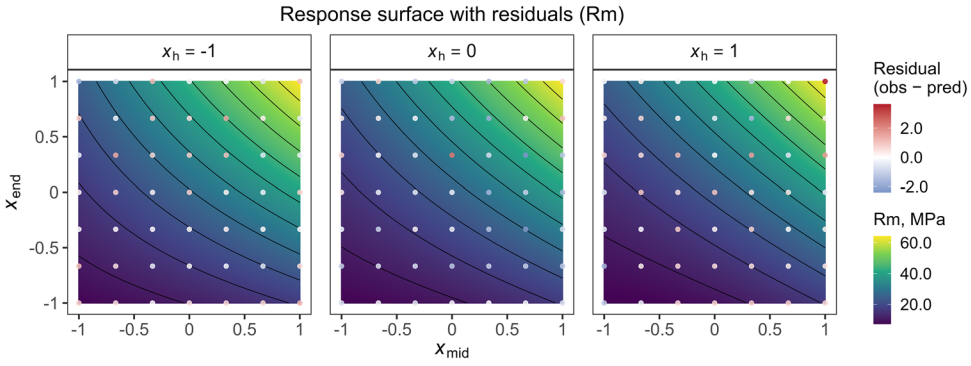

Fig. 12 Contour plot of the fitted response surface for R_m as a function of the centered and scaled geometric parameters. The overlaid points represent FEM simulation data, with point color indicating residuals between FEM-estimated values and response-surface predictions

Table 11 Results of the 10-fold cross-validation used to evaluate the predictive stability of the regression models within the investigated FEM design space

Response	RMSE (MPa)	MAE (MPa)	R^2_{CV}	NRMSE (%)
E	67.24	49.40	0.9968	1.22
$R_{p0.2}$	0.73	0.52	0.9972	1.20
R_m	0.95	0.74	0.9953	1.54

Table 12 Experimental validation results for the FEM-based regression models using effective diameters as input variables

Response	RMSE (MPa)	MAE (MPa)	R^2_{EXP}	NRMSE (%)
E	653.67	414.85	0.8594	9.52
$R_{p0.2}$	4.42	3.28	0.9029	7.96
R_m	5.06	4	0.8882	9.15

6.1 Validation of the regression models

To evaluate predictive performance of the regression models, a 10-fold cross-validation procedure was performed for the response surfaces of E, $R_{p0.2}$, and R_m. The results are shown in Table 11. All three responses have very high prediction accuracy. In particular, the cross-validated coefficient of determination R^2_{CV} is higher than 0.99, and the normalized root mean square error (NRMSE) stays below 2%. These results confirm that the proposed equations provide robust surrogate models for rapid screening and comparative assessment of lattice geometries within the investigated FEM design space.

To further examine how well the FEM-based regression models describe experimentally determined mechanical properties, an additional validation was carried out using the experimental dataset. The experimental results were compared against the developed regression models. As shown in Table 12, the agreement between model predictions and experimental measurements remained high for all three responses, with R^2_{EXP} values ranging from approximately 0.86 to 0.90. The prediction errors were higher than in cross-validation. This is expected, since the experimental comparison reflects not only model approximation error, but also actual manufacturing deviations, geometric imperfections, and experimental variability not captured in the idealized FEM data. Nevertheless, the obtained results support the practical usefulness of the regression models as predictive engineering tools. They also indicate that the highest accuracy is achieved when models are applied within the investigated FEM design space.

6.2 Back-transformed regression models

The back-transformed models are intended as surrogate equations suitable for early-stage design and geometry selection of tapered-strut BCC lattices within the investigated design space, where many candidate designs must be evaluated under limited time and computational resources. In this setting, Eqs. (4–6) can be used to rapidly estimate and compare candidate combinations of (d_{mid}, d_{end}, h) against stiffness and strength target values before performing detailed finite element analyses or manufacturing trials. Since Eqs. (4–6) are developed using FEM data and supported by a limited set of experiments, they should be interpreted as design screening tools rather than stand-alone predictive formulas for all as-built lattice specimens. Their use is therefore most appropriate for early-stage geometry selection, sensitivity analysis, and workflow acceleration within the investigated domain.

These equations capture nonlinear diameter effects, joint-node height effects, and their interactions. As a result, they can be used to investigate different design options and perform sensitivity analyses. This approach makes it easier to see how changes in tapering diameters and joint-node height affect E, $R_{p0.2}$, and R_m in design space. Their analytical form also allows their use in optimization workflows as approximate objective or constraint functions. In such workflows, detailed FEM analyses can still be used to verify accuracy. When supplemented by measured dimensional offsets from manufacturing, such as as-built diameters after PBF-LB, these equations may also support approximate as-built property screening. More broadly, the low computational cost of evaluating these equations may facilitate their future integration into design frameworks in which repeated

lattice-level FEM simulations would be impractical. In Eqs. (4–6), the geometric variables d_{mid}, d_{end}, and h are expressed in mm, while the predicted mechanical properties E, $R_{\mathrm{p0.2}}$, and R_{m} are expressed in MPa. Consequently, the units of the regression coefficients depend on the corresponding polynomial terms.

$$\begin{aligned} E = {} & 6937.43 - 10388.33\, d_{\mathrm{mid}} - 7632.32\, d_{\mathrm{end}} - 726.34\, h \\ & + 3114.04\, d_{\mathrm{mid}}^2 + 1932.48\, d_{\mathrm{end}}^2 + 8024.21\, d_{\mathrm{mid}} d_{\mathrm{end}} \\ & + 560.23\, d_{\mathrm{mid}} h + 448.44\, d_{\mathrm{end}} h. \end{aligned} \tag{4}$$

$$\begin{aligned} R_{\mathrm{p0.2}} = {} & 27.96 - 74.61\, d_{\mathrm{mid}} - 12.52\, d_{\mathrm{end}} + 3.93\, h \\ & + 20.94\, d_{\mathrm{mid}}^2 - 13.09\, d_{\mathrm{end}}^2 + 87.48\, d_{\mathrm{mid}} d_{\mathrm{end}} \\ & - 14.31\, d_{\mathrm{end}} h + 9.85\, d_{\mathrm{end}}^2 h. \end{aligned} \tag{5}$$

$$\begin{aligned} R_{\mathrm{m}} = {} & -22.36 + 3.20\, d_{\mathrm{mid}} + 25.76\, d_{\mathrm{end}} + 22.83\, h \\ & - 20.99\, d_{\mathrm{mid}}^2 - 26.67\, d_{\mathrm{end}}^2 + 84.09\, d_{\mathrm{mid}} d_{\mathrm{end}} \\ & - 30.52\, d_{\mathrm{mid}} h - 27.31\, d_{\mathrm{end}} h \\ & + 16.96\, d_{\mathrm{mid}}^2 h + 15.17\, d_{\mathrm{end}}^2 h. \end{aligned} \tag{6}$$

Overall, the developed regression models serve as a design map of the tensile response of tapered-strut BCC lattices within the investigated design space. They enable rapid comparative estimation at low computational cost and may support preliminary engineering decisions involving feasibility checks and iterative geometry refinement.

7 Conclusion

In this study, the tensile response of PBF-LB Ti6Al4V BCC lattices with tapered struts was investigated. The influence of unit-cell geometry was investigated by altering the end diameter d_{end}, mid-span diameter d_{mid}, and joint-node height h. The tensile test experiments were complemented by the finite element simulations using an elastoplastic model with ductile damage. Manufacturing-related diameter deviations were measured and implemented in the finite element models to support a consistent comparison.

Both experiments and simulations showed that stiffness and strength increased with increasing d_{mid} and d_{end}, with the largest gains obtained when both are increased simultaneously, confirming a strong geometric interaction. The numerical framework showed good overall agreement with the experiments in the elastic and early plastic regime, whereas larger differences appeared after peak load, where progressive failure, specimen-level variability, and manufacturing-related imperfections became more influential. A single set of mechanical properties was intentionally used across all investigated configurations to retain a simple and practically applicable modeling procedure. Within these assumptions, the experiments provided meaningful support for the main numerical trends across the investigated geometries, although the experimental dataset remained limited for some configurations and full failure characterization was not achieved for configuration 1-1-3.

Failure initiated in nodal regions in both approaches, although experimental fracture surfaces were often more complex than the planar patterns obtained numerically.

Based on a FEM parametric dataset, response surface models were developed for E, $R_{\mathrm{p0.2}}$, and R_{m}, capturing the dominant nonlinear effects of the tapering diameters and their interaction within the investigated design space. These models may serve as computationally efficient tools for preliminary geometry screening and comparative assessment, particularly when the focus is on elastic and early plastic response.

Future work will address the post-peak regime more explicitly by incorporating specimen-level geometric variability, surface roughness and porosity, and enhanced damage or instability modeling, as well as expanding experimental validation to additional geometries and loading conditions. Higher-resolution geometric characterization methods, such as CT or optical 3D reconstruction, may further improve specimen-specific numerical fidelity.

Acknowledgments The Laboratory for Advanced Mechatronics – LAMA FVG – of the University of Udine is gratefullyacknowledged for technical support. LAMA FVG is an international research center for product and process innovation wherethe three universities of Friuli Venezia Giulia (Italy) cooperate to promote R&D activities at the academic and industrial level.The authors are grateful to Robert Basan and Ela Marković at the Faculty of Engineering, University of Rijeka, for facilitatingaccess to the Galdabini tensile testing machine and DIC system, as well as for their technical support.

Author Contribution DL: conceptualization, methodology, numerical analysis, formal analysis, investigation, visualization, writing–original draft preparation, writing–review and editing. EV: conceptualization, methodology, investigation, resources, writing–review and editing. FS: investigation, data acquisition, formal analysis, writing–review and editing. MF: validation, methodology, writing–review and editing, supervision. GT: validation, resources, writing–review and editing, supervision. MS: conceptualization, validation, resources, writing–review and editing, supervision.

Funding Emanuele Vaglio received funding under the REACT EU Italian PON 2014–2020 Program – Action IV.4 – Innovation(DM 1062, 10/08/2021).

Data availability The datasets that support the findings of this study are not publicly available, but are available from the corresponding author upon reasonable request.

Declarations

Conflict of interest The authors declare no conflict of interest.

References

1. Bai L, Xu Y, Chen X, Xin L, Zhang J, Li K, Sun Y (2021) Improved mechanical properties and energy absorption of Ti6Al4V laser powder bed fusion lattice structures using curving lattice struts. Mater Des 211: 110140 (2021) https://doi.org/10.1016/j.matdes.2021.110140
2. Leary M, Mazur M, Williams H, Yang E, Alghamdi A, Lozanovski B, Zhang X, Shidid D, Farahbod-Sternahl L, Witt G, Kelbassa I, Choong P, Qian M, Brandt M (2018) Inconel 625 lattice structures manufactured by selective laser melting (SLM): Mechanical properties, deformation and failure modes. Mater Des 157(2017):179–199. https://doi.org/10.1016/j.matdes.2018.06.010
3. Peng C, Tran P, Nguyen-Xuan H, Ferreira AJM (2020) Mechanical performance and fatigue life prediction of lattice structures: parametric computational approach. Compos Struct 235:111821. https://doi.org/10.1016/j.compstruct.2019.111821
4. Lvov VA, Senatov FS, Shinkaryov AS, Chernyshikhin SV, Gromov AA, Sheremetyev VA (2023) Experimental 3D printed re-entrant auxetic and honeycomb spinal cages based on Ti-6Al-4 V: computer-Aided design concept and mechanical characterization. Compos Struct 310:116766. https://doi.org/10.1016/j.compstruct.2023.116766
5. Bruson D, Galati M, Calignano F, Iuliano L (2023) Mechanical characterisation and simulation of the tensile behaviour of polymeric additively manufactured lattice structures. Exp Mech 63(7):1117–1133. https://doi.org/10.1007/s11340-023-00976-5
6. Gomes RA, Musa IU, Sonego M, Gomes GF (2016) A comprehensive review of lattice structures: from design to energy absorption. Thin-Walled Struct 222:114478. https://doi.org/10.1016/j.tws.2026.114478
7. Bai L, Yi C, Chen X, Sun Y, Zhang J (2019) Effective design of the graded strut of BCC lattice structure for improving mechanical properties. Materials 12(13):2192. https://doi.org/10.3390/ma12132192
8. Kang J, Dong E, Li D, Dong S, Zhang C, Wang L (2020) Anisotropy characteristics of microstructures for bone substitutes and porous implants with application of additive manufacturing in orthopaedic. Mater Des 191: 108608 (2020) https://doi.org/10.1016/j.matdes.2020.108608
9. Ren X, Xiao L, Hao Z (2019) Multi-property cellular material design approach based on the mechanical behaviour analysis of the reinforced lattice structure. Mater Design 174:107785. https://doi.org/10.1016/j.matdes.2019.107785
10. Drücker S, Schulze M, Ipsen H, Bandegani L, Hoch H, Kluge M, Fiedler B (2021) Experimental and numerical mechanical characterization of additively manufactured Ti6Al4V lattice structures considering progressive damage. Int J Mech Sci 189:105986. https://doi.org/10.1016/j.ijmecsci.2020.105986
11. Kornfellner E, Reininger S, Geier S, Schwentenwein M, Benca E, Scheiner S, Moscato F (2024) Mechanical properties of additively manufactured lattice structures composed of zirconia and hydroxyapatite ceramics. J Mech Behav Biomed Mater 158:106644. https://doi.org/10.1016/j.jmbbm.2024.106644
12. Kolken HMA, Janbaz S, Leeflang SMA, Lietaert K, Weinans HH, Zadpoor AA (2018) Rationally designed meta-implants: a combination of auxetic and conventional meta-biomaterials. Mater Horiz 5(1):28–35. https://doi.org/10.1039/c7mh00699c
13. Surmeneva MA, Surmenev RA, Chudinova EA, Koptioug A, Tkachev MS, Gorodzha SN, Rännar LE (2017) Fabrication of multiple-layered gradient cellular metal scaffold via electron beam melting for segmental bone reconstruction. Mater Des 133:195–204. https://doi.org/10.1016/j.matdes.2017.07.059
14. Danesh H, Heußen L, Montáns FJ, Reese S, Brepols T (2025) A two-scale computational homogenization approach for elastoplastic truss-based lattice structures. Results Eng 25:103976. https://doi.org/10.1016/j.rineng.2025.103976
15. Gebre NM, De Biasi R, Rita DA, Santus C, Romanelli L, Neri P, Perini M, Berto F, Benedetti M (2025) Towards standardization of tensile testing for strut-based lattices using compensated beam modeling and strain-energy-based optimization. Mater Design 258:114696. https://doi.org/10.1016/j.matdes.2025.114696
16. Kostadinov A, Yan L, Teo AQA, O'Neill G (2021) Slanted and cluttered: solving deficiencies in SLM-manufactured lattice geometries. Mater Design 211:110130. https://doi.org/10.1016/j.matdes.2021.110130
17. Aiza I, Baldi C, Vega FM, Sebastiani S, Veronese NE, Yousefi M, Mosallanejad MH, Maleki E, Guagliano M, Iuliano L, Saboori A, Bagherifard S (2025) Effects of build orientation and inclined features on physical, microstructural and mechanical properties of powder bed fusion additively manufactured metallic parts. Prog Mater Sci 147:101357. https://doi.org/10.1016/j.pmatsci.2024.101357
18. Jung J, Meyer G, Greiner M, Mittelstedt C (2023) Load introduction specimen design for the mechanical characterisation of lattice structures under tensile loading. J Manuf Mater Proc 7(1):37. https://doi.org/10.3390/jmmp7010037
19. Cibrario L, Gastaldi C, Delprete C, Cozza IF (2025) Mechanical design of lattice metamaterials: a multiscale homogenization-based operational procedure. Mater Design 251:113614. https://doi.org/10.1016/j.matdes.2025.113614
20. Herrnböck L, Steinmann P (2022) Homogenization of fully nonlinear rod lattice structures: on the size of the RVE and micro structural instabilities. Comput Mech 69(4):947–964. https://doi.org/10.1007/s00466-021-02123-0
21. Nguyen V-D, Noels L (2014) Computational homogenization of cellular materials. Int J Solids Struct 51(11–12):2183–2203. https://doi.org/10.1016/j.ijsolstr.2014.02.029
22. Geng Y, Harrison N (2019) Functionally graded bimodal Ti6Al4V fabricated by powder bed fusion additive manufacturing: crystal plasticity finite element modelling. Mater Sci Eng A 733:138736. https://doi.org/10.1016/j.msea.2019.138736
23. Zhao M, Liu F, Fu G, Zhang D, Zhang T, Zhou H (2018) Improved mechanical properties and energy absorption of BCC lattice structures with triply periodic minimal surfaces fabricated by SLM. Materials 11(12):2411. https://doi.org/10.3390/ma11122411
24. Zhao M, Zhang DZ, Li Z, Zhang T, Zhou H, Ren Z (2022) Design, mechanical properties, and optimization of BCC lattice structures with taper struts. Compos Struct 295(April):115830. https://doi.org/10.1016/j.compstruct.2022.115830
25. Li J, Luo Z, Guo Y, Yan Z, Wang Y (2025) Quasi-Static compression and tensile behavior of additively manufactured Al-Mg-Sc-Zr alloy lattices: the role of cell topology. Metals 15(11):1255. https://doi.org/10.3390/met15111255
26. Berthel J, Beuth J, Panat R (2026) Geometric deviations and their effects in thin-plate lattice structures fabricated via LPBF. Additive Manuf 119:105117. https://doi.org/10.1016/j.addma.2026.105117

27. Pelegatti M, Scalzo F, Sordetti F, Vaglio E, Magnan M, Totis G, Sortino M, Benasciutti D, Lanzutti A, De Bona F, Salvati E (2024) Low cycle fatigue behaviour of cellular materials: experimental comparative study of strut-based and gyroid structures made of additively manufactured 316L steel. Int J Fatigue 178:108024. https://doi.org/10.1016/j.ijfatigue.2023.108024
28. Viale V, Stavridis J, Salmi A, Bondioli F, Saboori A (2022) Optimisation of downskin parameters to produce metallic parts via laser powder bed fusion process: an overview. Int J Adv Manuf Technol 123(7–8):2159–2182. https://doi.org/10.1007/s00170-022-10314-z
29. Systèmes D, Corp S Abaqus 2020 Documentation. (2020). Dassault Systèmes Simulia Corp
30. Simo JC, Hughes TJR (1998) Computational inelasticity. Springer, New York . https://doi.org/10.1007/b98904
31. Murchio S, Dallago M, Zanini F, Carmignato S, Zappini G, Berto F, Maniglio D, Benedetti M (2021) Additively manufactured Ti–6Al–4V thin struts via laser powder bed fusion: effect of building orientation on geometrical accuracy and mechanical properties. J Mech Behav Biomed Mater 119:104495. https://doi.org/10.1016/j.jmbbm.2021.104495
32. Louw DF, Neaves M, Becker TH (2026) The effect of residual stress on the fracture toughness of Ti–6Al–4V produced by laser-based powder bed fusion. Int J Fract 250(1):7. https://doi.org/10.1007/s10704-025-00906-7
33. Pasang T, Tavlovich B, Yannay O, Jackson B, Fry M, Tao Y, Turangi C, Wang J-C, Jiang C-P, Sato Y, Tsukamoto M, Misiolek WZ (2021) Directionally-dependent mechanical properties of Ti6Al4V manufactured by electron beam melting (EBM) and selective laser melting (SLM). Materials 14(13):3603. https://doi.org/10.3390/ma14133603
34. R Core Team: R: A language and environment for statistical computing. R foundation for statistical computing, Vienna, Austria (2024). R Foundation for Statistical Computing. https://www.R-project.org/